Supporting Information

Prussian Blue/RGO with Less Coordinated Water as Superior Cathode Material for Sodium-Ion Batteries

Dezhi Yang, Jing Xu, Xiao-Zhen Liao,* Hong Wang, Yu-Shi He and Zi-Feng Ma*

S1. Experimental

In a typical synthesis of PB, 1 M $Na_4Fe(CN)_6$ was dissolved in 0.1 M H_2SO_4 aqueous solution at room temperature and then maintained at 80°C for 3 h to form micro-cubic PB particles. The solid product was collected by centrifugation and washed six times with Milli-Q water. The final PB product was then dried in a vacuum oven. The GO was synthesised by a modified Hummer's method.[1] To prepare GOPCs, the GO and PB were stirred together in an aqueous solution to form slurries with different GO and PB contents. Thereafter, the slurries were ultrasonically dispersed for 10 min, and then spray-dried to obtain the GOPCs. The dried GOPCs were heated under an air atmosphere at 220°C for 3 h to form RGOPCs.

For a typical coin cell, the cathodes were composed of 70 wt.% active material (PB or RGOPCs), 20 wt.% super P, and 10 wt.% polyvinylidene fluoride (PVDF). The cathode active material loading was 3-4 mg cm^{-2}. The cathodes were incorporated into coin cells (R2016) with sodium metal foil as the anode and 1.0 M $NaClO_4$/EC+DMC (1:1, v/v) as the electrolyte in an argon-filled glove box.

The morphologies of the samples were analysed by scanning electron microscopy (Sirion 200, FEI Company). The structural characteristic of the samples were measured by the X-ray diffraction (D/max-2200/PC, Rigaku Co., Ltd.) in equal 2θ steps of 0.02° using a Cu Kα radiation. The chemical composition was examined by elemental analysis (Vario-EL Cube, Elementar Analysensysteme) for C and N and by inductively coupled plasma analysis (iCAP 6000 Radial, Thermo Fisher Scientific, Inc.) for Fe and Na. TG analysis was conducted on a DSC/DTA-TG instrument (STA 449 F3 Jupiter, NETZSCH-Gerätebau GmbH) at a heating rate of 5°C/min under an atmospheric environment. FT-IR and Raman spectra were recorded using an FT-IR spectrophotometer (Spectrum 100, PerkinElmer Inc.)

and a DXR Raman Microscope (DXR, Thermo Fisher Scientific, Inc.) equipped with an argon-ion laser (633 nm), respectively.

The galvanostatic charge-discharge tests were conducted using a battery test system (Land CT2001A model, Wuhan Jinnuo Electronics Co., Ltd.). All cyclic voltammetric experiments were performed on a CHI electrochemical workstation (CHI 670D, CHI Instrument Co.). Electrochemical impedance spectroscopy (EIS) was performed using Solartron equipment (SI 1287 + SI 1260, Solartron Analytical, Ltd.) within a frequency range of 0.1 Hz to 100 kHz at the open-circuit potential. The amplitude of the alternating voltage was 5 mV. All electrochemical experiments were carried out at 25°C.

S2. The thermo gravimetric (TG) analysis of GO, PB, RGOPC1, RGOPC2 and RGOPC3

Fig. S1a shows the thermo gravimetric (TG) curve of GO. Obviously, the oxide groups on the GO are decomposed at about 220℃ and resulting the weight loss of GO which are consist with the reference.[2] Fig. S1b shows the TG curve and the differential scanning calorimetric (DSC) curve of PB. PB will begin to slight decompose when the temperature is increased to above 240℃. Thus, the weight loss of PB below 240℃ is mainly attributed to absorbed water and zeolitic water. The water content in PB was sensed to be 11.5 wt.%. Fig. S1c, S1d and S1f show the thermo gravimetric (TG) curve of RGOPC1, RGOPC2 and RGOPC3, respectively. The weight losses of RGOPC1, RGOPC2 and RGOPC3 at 240℃ were 8.6 wt.%, 6 wt.% and 5.1 wt.%, respectively. However, the water contents in these samples cannot be detected precisely which is due to the mild decomposition of RGO.

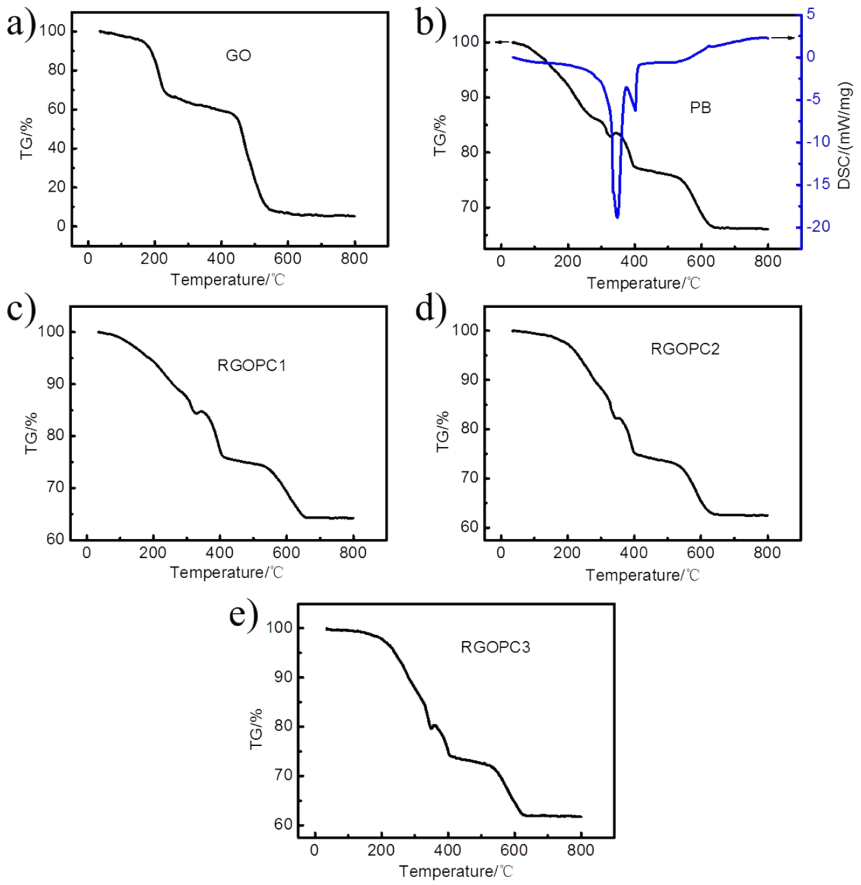

Figure S1. (a) The thermo gravimetric (TG) curve of GO. (b) The thermo gravimetric (TG) curve and the differential scanning calorimetric (DSC) curve of PB. The thermo gravimetric (TG) curves of RGOPC1 (c), RGOPC2 (d) and RGOPC3 (f). All TG and DSC tests were performed under atmospheric environment.

S3. The SEM images of RGOPC3 and GOPC3

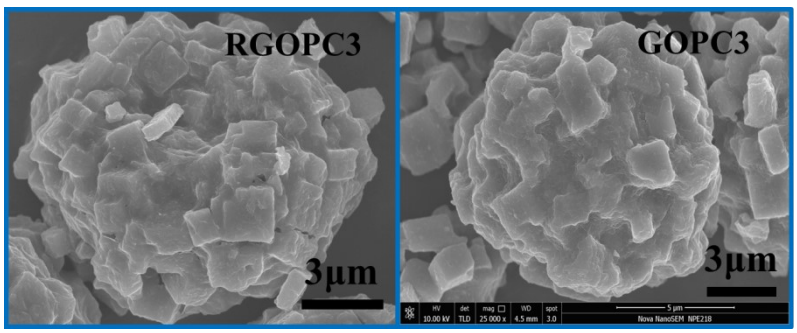

Figure S2. The SEM images of RGOPC3 and GOPC3.

S4. Cyclic voltammograms, FT-IR spectra of PB and RGOPCs

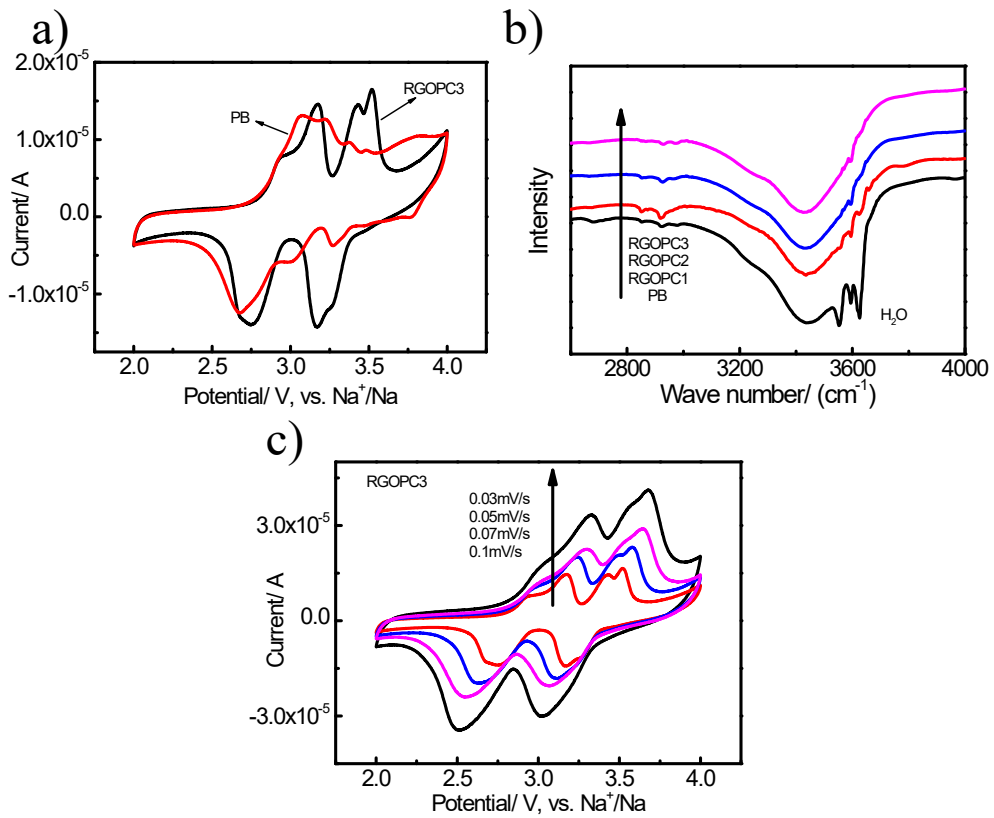

Figure S3. (a) Cyclic voltammograms of PB and RGOPC3 recorded at a scan rate of 0.03 mV/s between 2 V and 4 V. (b) FT-IR spectra of PB, RGOPC1, RGOPC2 and RGOPC3. (c) The Cyclic voltammograms of RGOPC3 at different scan rate between 2V and 4V.

S5. The Rietveld refinement results of the XRD patterns (PB and RGOPCs)

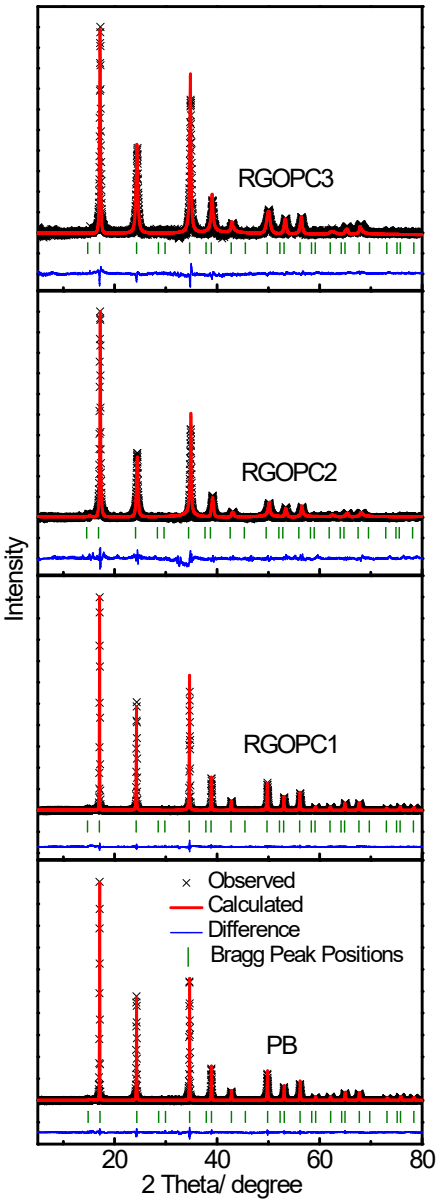

Figure S4. Rietveld refined room temperature XRD patterns of PB, RGOPC1, RGOPC2 and RGOPC3.

Table S1. The occupation of the atoms and d-spacing of PB, RGOPC1, RGOPC2 and RGOPC3.

	PB	RGOPC1	RGOPC2	RGOPC3
Fe2	1	1	1	1
Fe1	0.79	0.79	0.79	0.79
Na	0.81	0.81	0.81	0.81
C	0.802	0.791	0.734	0.703
N	0.802	0.791	0.734	0.703
O	0.307	0.284	0.103	0.091
D-spacing	10.3423Å	10.3361Å	10.2735Å	10.2591Å
Rp	4.22%	4.41%	5.36%	5.22%
Rwp	5.02%	5.83%	7.14%	6.47%

S6. The functions of GO during the co-heating process for removing coordinated water

To verifying the functions of GO during the co-heating process for removing coordinated water, we first analyzed the FT-IR spectra of the PB before and after heating at the same conditions (Figure S5a). Only tiny differences were observed. The PB after heating still presents the peaks belonging to H_2O at 3556 cm^{-1}, 3594 cm^{-1} and 3627 cm^{-1} obviously. From the charge/discharge curve of PB after heating (Figure S5b), one discharge platform was delivered. From the Raman spectra (Figure S5c), the ratios of $Fe(CN)_6^{4-}$/ $Fe(CN)_6^{3-}$ were similar. Hence, the coordinated water cannot be removed under simple heating process for PB without GO. On the other hand, the peaks of coordinated water on the FT-IR spectra of GOPC3 and RGOPC3 (Figure S5d), were significantly decreased. The ratios of $Fe(CN)_6^{4-}$/ $Fe(CN)_6^{3-}$ for RGOPC3 was also decreased (Figure S5f). Thus, the original GO applied to covering PB played pivotal roles in the heating process.

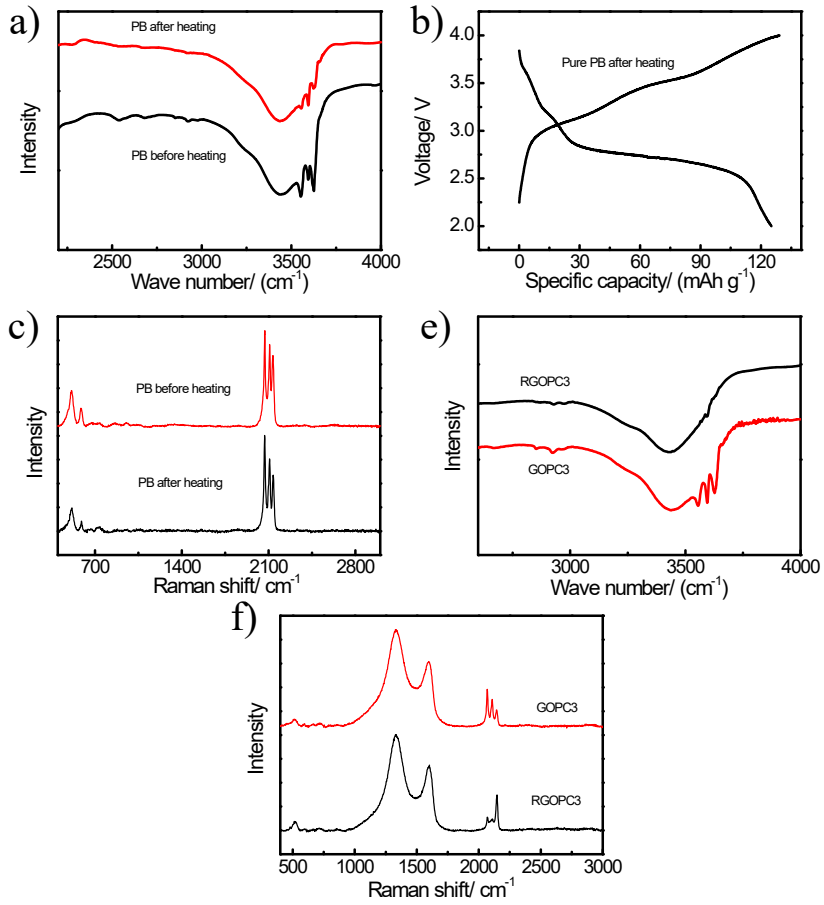

Figure S5. (a) The FT-IR spectra of PB before and after heating. (b) The charge/discharge curves of PB after heating between 2V-4V at 30 mA/g. (c) The Raman spectra of PB before and after heating. (d) The IR spectra and (f) the Raman spectra of GOPC3 and RGOPC3.

As GO is consists of graphene and oxide groups, in order to explore the thermal reaction mechanism of the GO/PB composite during co-heating, the GO/PB composite with 9wt.% GO content (GOPC3-1) and the graphene/PB composite with 9wt.% graphene content (GPC3-1) were both heated under 220℃ with the same conditions to point out the role of graphene and oxide groups directly. The graphene was highly reduced graphene oxide. The GPC3-1 cannot be synthesized by spray drying because the PB and graphene would separate rather than to form composite during spray drying. Thus, the GOPC3-1 and GPC3-1 were synthesized by the solution-evaporation method. For synthesis of GOPC3-1, the 9 wt.% GO and 91wt.% PB were stirred together in the aqueous solutions, and then evaporated at 80℃ and under stirring to form dried film. For GPC3-1, the synthetic process is similar where just replacing the GO by the highly reduced graphene oxide. The fabricated films were heated

under atmosphere and at 220℃ for 3h, and ball milled and dried again as cathode materials. Fig. S6a and S6b show the charge/discharge curves of RGOPC3-1 and GPC3-1after heating. The GPC3-1 after heating only delivered one voltage platform of Fe2. That is to say, the oxide groups are necessary for the original composites to remove coordinating water. We also performed the charge/discharge curves of RGOPC3 heated at 180℃ (Figure S6c). The GOPC3 heated at 220℃ (RGOPC3) delivered two distinct voltage platforms of Fe1 and Fe2. But the GOPC3 heated at 180℃ presents one voltage platform of Fe2. The oxide groups on the GO would decompose at 220℃ but kept stable at 180℃. Hence, the decomposition of oxide groups on the GO is essential to induce the removing of coordinated water. In the GOPC, the GO covered the surface of PB well indicating that the decomposition of oxide groups also happens on the PB surface at 220℃.

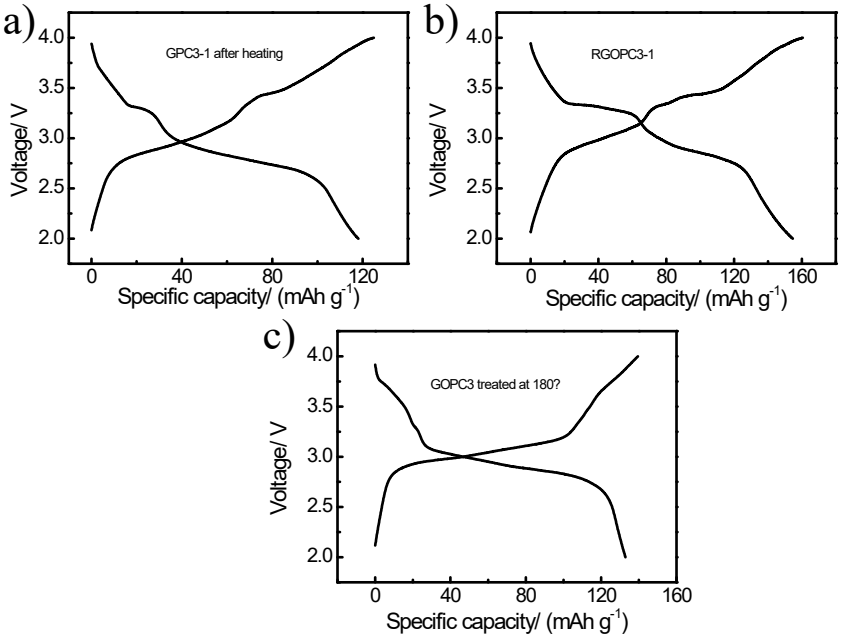

Figure S6. The charge/discharge curves of (a) GPC3-1 and (b) RGOPC3-1 after heating between 2V-4V at 30 mA/g. (c) The charge/discharge curves of GOPC3 (heated at 180℃) between 2V-4V at 30 mA/g.

S7. The charge/discharge curve of RGO

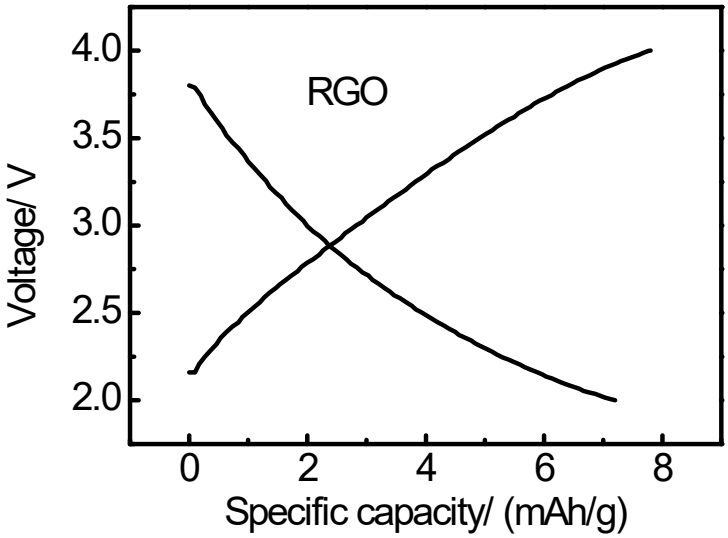

Figure S7. The galvanostatic charge–discharge profiles of RGO between 2.0V-4.0V at 30 mA/g.

S8. The first charge/discharge curves of PB and RGOPCs

In the first charge/discharge curves of PB and RGOPCs (Figure S8), we can see that the first discharge capacities of PB, RGOPC1, RGOPC2 and RGOPC3 were 71 mAh/g, 79.9 mAh/g, 90.1 mAh/g and 100.3 mAh/g, respectively. In other words, the initial valence states of redox ions in these four samples are different. It is consist with the Raman spectra of PB and RGOPCs in Figure 4.

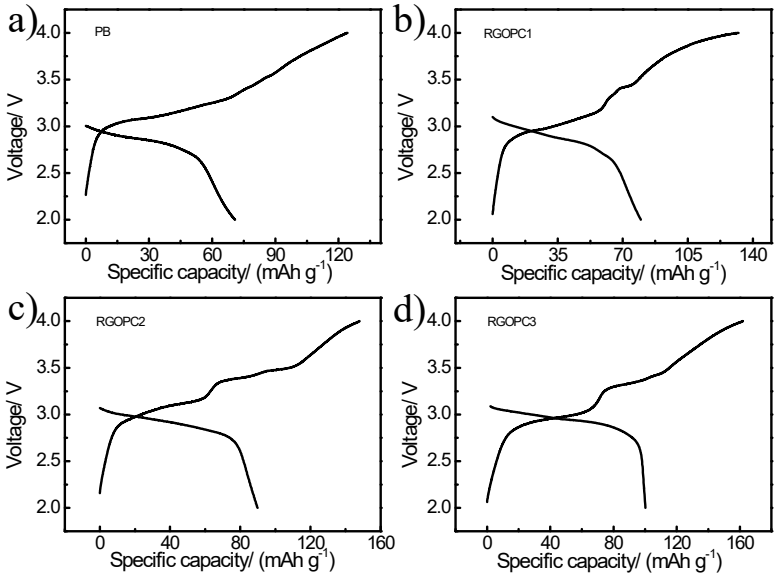

Figure S8. The first galvanostatic charge–discharge profiles of PB, RGOPC1, RGOPC2 and RGOPC3 between 2.0V-4.0V at 30 mA/g.

S9. The ratios of $Fe(CN)_6^{4-}/Fe(CN)_6^{3-}$ of PB, RGOPC1, RGOPC2 and RGOPC3

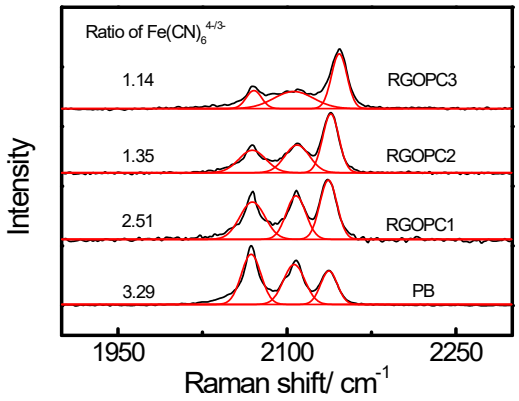

Figure S9. The Raman spectra of PB, RGOPC1, RGOPC2 and RGOPC3. The red lines are fitting results.

S10. The Raman spectra of RGOPC3 with different heating times

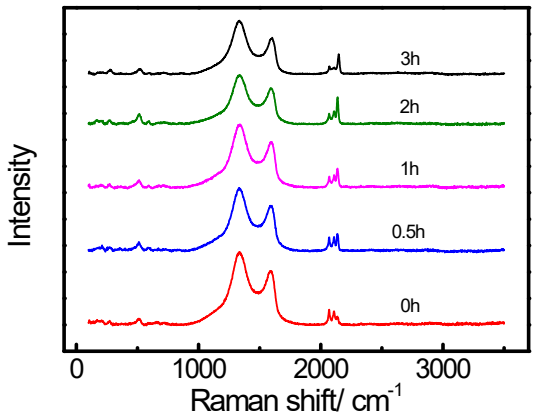

Figure S10. The Raman spectra of RGOPC3 with different heating times.

S11. The charge/discharge curve and the FT-IR spectra of RGOPC3 treated by water and dried again

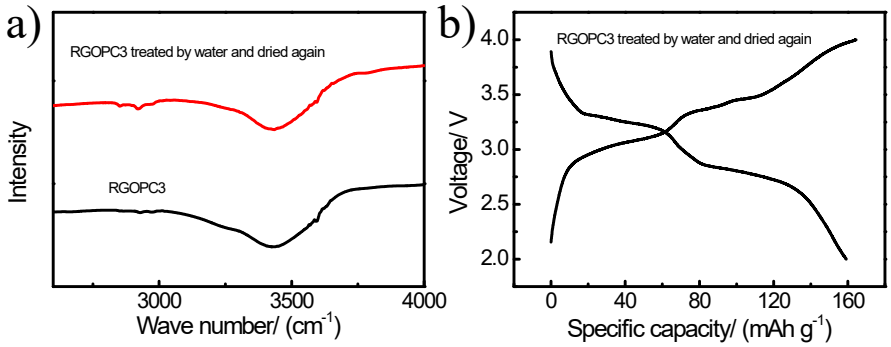

Figure S11. The IR spectra (a) and the charge/discharge curve (b) of RGOPC3 treated by water and dried again

S12. The discharge curves of RGOPC3 and the Nyquist plots of PB and RGOPCs

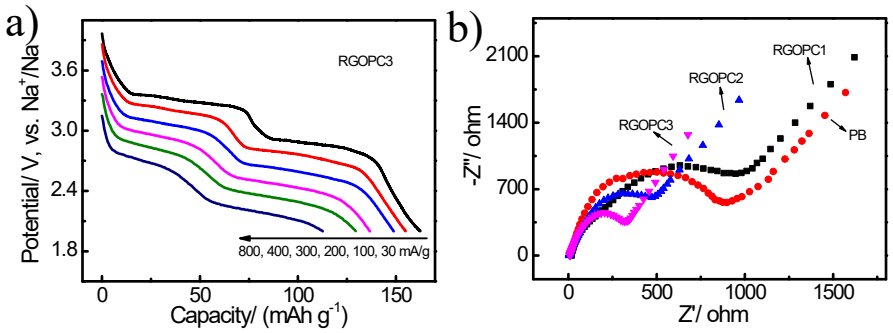

Figure S12. (a) The galvanostatic discharge curves of RGOPC3 at different current densities between 2 V and 4 V. (b) The Nyquist plots of the sodium-ion cells with PB, RGOPC1, RGOPC2 and RGOPC3 as cathodes after ten charge/discharge cycles at 200 mA/g.

References:

1. X. Yang, L. Qiu, C. Cheng, Y. Wu, Z.-F. Ma and D. Li, *Angew. Chem. Int. Ed.*, 2011, **50**, 7325.

2. G.-W. Zhou, J. Wang, P. Gao, X. Yang, Y.-S. He, X.-Z. Liao, J. Yang and Z.-F. Ma, *Ind. Eng. Chem. Res.*, 2013, ***52***, 1197.

Table S2 The comparison of representative Prussian blue analogue materials for sodium-ion batteries.

Composition Synthesis method	Size (μm)	Reversible capacity in Na cells (mAh g^{-1} / mA g^{-1})	Rate Performance (mAh g^{-1})	Cycle life
$Na_{0.61}Fe[Fe(CN)_6]_{0.94}\cdot 2.79H_2O$[1] Acid-assisted single iron-source	0.3-0.6	170 / 25	70 mAh g^{-1} / 600 mA g^{-1}	100%@150th at 25 mA g^{-1}
$Na_{1.56}FeFe(CN)_6\cdot 3.1H_2O$[2] Acid-assisted single iron-source	0.5-3	103.6 / 20	90 mAh g^{-1} / 100 mA g^{-1}	97%@400th at 20 mA g^{-1}
$Na_{1.63}Fe[Fe(CN)_6]_{0.89}$[3] Acid-assisted single iron-source	1-3	150 / 25	N.A.	90%@200th at 25 mA g^{-1}
$Na_{0.52}Fe[Fe(CN)_6]_{0.95}\cdot 4.00H_2O$[4] Acid-assisted single iron-source	~0.4	117 / 200	98.3 mAh g^{-1} / 2000 mA g^{-1}	91%@1380th at 25 mA g^{-1}
Dehydrated $Na_{1.92}FeFe(CN)_6$[5] Acid-assisted single iron-source	0.8-4	160 / 10	145 mAh g^{-1} / 1500 mA g^{-1}	80%@750th at 300 mA g^{-1}
$Na_{1.73}Fe[Fe(CN)6]_{0.98}$[6] Simple co-precipitation	0.06-0.1	123 / 100	78 mAh g^{-1} / 800 mA g^{-1}	73%@200th at 100 mA g^{-1}
$Na_{1.70}FeFe(CN)_6$[7] Citrate as chelating agent	~0.05	129 / 200	71.2 mAh g^{-1} / 1200 mA g^{-1}	70.5%@100th at 200 mA g^{-1}
$Na_{1.95}Fe[Fe(CN)_6]_{0.93}\cdot\square_{0.07}$[8] Citrate as chelating agent	3-4	~120 / 50	60 mAh g^{-1} / 1600 mA g^{-1}	79%@280th at 100 mA g^{-1}
$Na_{1.73}Fe[Fe(CN)_6]\cdot 3.8H_2O$[9] Citrate as chelating agent	~1.25	116 / 10	70 mAh g^{-1} / 2000 mA g^{-1}	71%@500th at 100 mA g^{-1}
$Na_{1.76}FeFe(CN)_6\cdot 2.6H_2O$[10] Citrate as chelating agent	~3	115 / 50	~76 mAh g^{-1} /4000 mA g^{-1}	76%@1000th at 200 mA g^{-1}
$Na_{0.71}Fe[Fe(CN)_6]_{0.82}\cdot 2.68H_2O$[11]	~0.1	151 / 100	90 mAh g^{-1}	82%@100th

Citrate as chelating agent			/3200 mA g^{-1}	at 100 mA g^{-1}
$Na_{1.81}Fe[Fe(CN)_6]_{0.83}\cdot 2.04H_2O$[12] Citrate as chelating agent	~0.2	140 / 28	90 mAh g^{-1} /1400 mA g^{-1}	79.7%@3700th at 700 mA g^{-1}
$Na_{1.51}Fe[Fe(CN)_6]_{0.87}\cdot 1.83H_2O$[13] Ball milling	5	124.2 /17	84.1 mAh g^{-1} /3400 mA g^{-1}	65.3%@1000th at 170 mA g^{-1}
$Na_{1.59}Fe[Fe(CN)_6]_{0.95}\cdot \square_{0.05}\cdot 1.92H_2O$[14] Ball milling	~0.4	~130 / 28	118 mAh g^{-1} /1400 mA g^{-1}	85%@100th at 140 mA g^{-1}
$Na_{1.56}Ni_{0.32}Fe_{0.68}[Fe(CN)_6]_{0.89}\cdot \square_{0.11}$[15] Soaking coating	2-3	114 / 50	68 mAh g^{-1} / 400 mA g^{-1}	60%@800th at 300 mA g^{-1}
$Na_{1.36}FeFe(CN)_6$@PDA[16] PDA Coating	~0.1	118.6 / 200	72.2 mAh g^{-1} / 5000 mA g^{-1}	77.4%@500th at 200 mA g^{-1}
$Na_{0.97}FeFe(CN)_6$/CNTs[17]	—	149.2 /17	68.6 mAh g^{-1} / 3400 mA g^{-1}	92%@500th at 700 mA g^{-1}
$Na_{0.81}Fe[Fe(CN)_6]_{0.79}*\square_{0.21}$/RGO in this work	1-3	163.3/30	112 mAh g^{-1} /800 mA g^{-1}	91.9%@500th at 200 mA g^{-1}

References:

1. Y. You, X.-L. Wu, Y.-X. Yin and Y.-G. Guo, *Energy & Environmental Science*, 2014, **7**, 1643-1647.

2. W.-J. Li, S.-L. Chou, J.-Z. Wang, Y.-M. Kang, J.-L. Wang, Y. Liu, Q.-F. Gu, H.-K. Liu and S.-X. Dou, *Chemistry of Materials*, 2015, **27**, 1997-2003.

3. Y. You, X. Yu, Y. Yin, K.-W. Nam and Y.-G. Guo, *Nano Research*, 2015, **8**, 117-128.

4. J. Hu, H. Tao, M. Chen, Z. Zhang, S. Cao, Y. Shen, K. Jiang and M. Zhou, *ACS Applied Materials & Interfaces*, 2022, **14**, 12234-12242.

5. L. Wang, J. Song, R. Qiao, L. A. Wray, M. A. Hossain, Y.-D. Chuang, W. Yang, Y. Lu, D. Evans, J.-J. Lee, S. Vail, X. Zhao, M. Nishijima, S. Kakimoto and J. B. Goodenough, *Journal of the American Chemical Society*, 2015, **137**, 2548-2554.

6. Y. Yang, E. Liu, X. Yan, C. Ma, W. Wen, X.-Z. Liao and Z.-F. Ma, *Journal of The Electrochemical Society*, 2016, **163**, A2117.

7. Y. Liu, Y. Qiao, W. Zhang, Z. Li, X. Ji, L. Miao, L. Yuan, X. Hu and Y. Huang, *Nano Energy*, 2015, **12**, 386-393.

8. Y. Huang, M. Xie, J. Zhang, Z. Wang, Y. Jiang, G. Xiao, S. Li, L. Li, F. Wu and R. Chen, *Nano Energy*, 2017, **39**, 273-283.

9. W. Wang, Y. Gang, Z. Hu, Z. Yan, W. Li, Y. Li, Q.-F. Gu, Z. Wang, S.-L. Chou, H.-K. Liu and S.-X. Dou, *Nature Communications*, 2020, **11**, 980.

10. W. Wang, Z. Hu, Z. Yan, J. Peng, M. Chen, W. Lai, Q.-F. Gu, S.-L. Chou, H.-K. Liu and S.-X. Dou, *Energy Storage Materials*, 2020, **30**, 42-51.

11. Z. G. Neale, C. Liu and G. Cao, *Sustainable Energy & Fuels*, 2020, **4**, 2884-2891.

12. C. Yan, A. Zhao, F. Zhong, X. Feng, W. Chen, J. Qian, X. Ai, H. Yang and Y. Cao, *Electrochimica Acta*, 2020, **332**, 135533.

13. C.-M. Xu, J. Peng, X.-H. Liu, W.-H. Lai, X.-X. He, Z. Yang, J.-Z. Wang, Y. Qiao, L. Li and S.-L. Chou, *Small Methods*, 2022, **6**, 2200404.

14. P. Zhang, C. Xu, J. Zhao, Y. Ma, X. Hu, L. Hao, X. Li, Y. Yang, S. Xu, H. Liu and Y.-S. Hu, *Materials Today Energy*, 2022, **27**, 101027.

15. Y. Zhou, Y. Jiang, Y. Zhang, Y. Chen, Z. Wang, A. Liu, Z. Lv and M. Xie, *ACS Applied Materials & Interfaces*, 2022, **14**, 32149-32156.

16. Y. Liu, D. He, Y. Cheng, L. Li, Z. Lu, R. Liang, Y. Fan, Y. Qiao and S. Chou, *Small*, 2020, **16**, 1906946.

17. P. Wan, H. Xie, N. Zhang, S. Zhu, C. Wang, Z. Yu, W. Chu, L. Song and S. Wei, *Advanced Functional Materials*, 2020, **30**, 2002624.